Combustion Theory and Modelling
Vol. 12, No. 6, 2008, 1125–1152

Taylor & Francis
Taylor & Francis Group

Unsteady simulation of a $CO/H_2/N_2$/air turbulent non-premixed flame

E. Giacomazzi,[a,*] F.R. Picchia,[a] N. Arcidiacono,[a] D. Cecere,[a] F. Donato[b] and B. Favini[b]

[a] *ENEA, ENE-IMP, S.P. 081, Via Anguillarese 301, 00123 – S.M. Galeria, Rome, Italy;* [b] *Department of Mechanics and Aeronautics, University 'La Sapienza', Via Eudossiana 18, 00184 – Rome, Italy*

(*Received 21 February 2008; final version received 3 June 2008*)

The Sandia/ETH-Zurich $CO/H_2/N_2$ non-premixed unconfined turbulent jet flame (named 'Flame A') is numerically simulated by solving the unsteady compressible reactive Navier–Stokes equations in a three-dimensional axisymmetric formulation, hence, in a formally two-dimensional domain. The turbulent combustion closure model adopted is the Fractal Model, FM, developed as a subgrid scale model for Large Eddy Simulation. The fuel is injected from a straight circular tube and the corresponding Reynolds number is 16 700, while the air coflows. Since the thickness of the nozzle is 0.88 mm, and the injection velocity high, $\sim$104 m s^{-1}, capturing the stabilization mechanism of the actual flame requires high spatial resolution close to the injector. Results are first obtained on a coarse grid assuming a fast-chemistry approach for hydrogen oxidation and a single step mechanism for carbon monoxide oxidation. With this approach the flame is inevitably anchored. Then, to understand the actual flame stabilization a more complex chemical mechanism, including main radical species, is adopted. Since using this chemistry and the coarse grid of previous simulation the flame blows off numerically, attention is focused on understanding the actual flame stabilization mechanism by simulating a small spatial region close to the injection with a very fine grid. Then, analysing these results, an artificial anchoring mechanism is developed to be used in simulations of the whole flame with a coarse grid. Unsteady characteristics are shown and some averaged radial profiles for temperature and species are compared with experimental data.

Keywords: syngas; flame anchoring; preferential diffusion; unsteady analysis; nonpremixed combustion

1. Introduction

The study of turbulent combustion requires the analysis of two main issues: turbulence coupled with chemical kinetics, and the understanding of how they interact. The multiscale interaction between fluid dynamics and chemistry has been investigated both computationally and experimentally. Large Eddy Simulation (LES) is an attractive numerical tool for the study of turbulence. Although LES offers great advantages with respect to RANS simulations in terms of physical content, particular issues may be hidden by commonly used and accepted 'tricks'. For example, it is not rare to find simulations of turbulent flames artificially anchored by means of temperature hot spots or flamelet profiles at inflow boundary [1]. This practice has the advantage of reducing high spatial resolution requirements in regions of the flow where anchoring is due to very fine turbulent structures that mix reactants and hot products at scales so fine that they are impossible to capture on coarse computational grids. On the other hand, this practise inevitably makes it

*Corresponding author. E-mail: eugenio.giacomazzi@casaccia.enea.it

ISSN: 1364-7830 print / 1741-3559 online

DOI: 10.1080/13647830802276131
http://www.tandf.co.uk/journals

impossible to investigate flame anchoring and, at the same time, it changes the dynamic behaviour of the flame, thus reducing the physical value of LES results.

Experimental databases available in the literature provide data on several flames that can be simulated numerically to investigate the coupling between fluid dynamics and combustion. The present work is on the numerical simulation of the so-called 'Flame A' included in the Sandia/ETH-Zurich database [2, 3] and is an introduction to a future Large Eddy Simulation. The numerical issues previously described about flame anchoring arise for this flame. The test case chosen is a $CO/H_2/N_2$ non-premixed, unconfined, turbulent jet flame. The fuel is injected at 292 K from a straight circular tube with squared-off ends (the inner diameter is 4.58 mm, while the outer diameter is 6.34 mm). Its injection bulk velocity is $76\,\mathrm{m\,s^{-1}}$ and the corresponding Reynolds number is 16 700. It is observed that the effective maximum velocity at the exit of the injector is about $104\,\mathrm{m\,s^{-1}}$. The air, at 290 K and wet (molar fraction of water 0.012), coflows at $0.75\,\mathrm{m\,s^{-1}}$. The percentage syngas composition is 40/30/30 in volume. The fuel tubing length is sufficient to make the assumption of fully developed turbulent pipe flow appropriate.

This test case, despite its simple geometry, can be useful to test combustion models and understand turbulence–chemistry interaction. The use of syngas as fuel facilitates validation because syngas adds only a modest increment in chemical kinetics complexity with respect to hydrogen combustion, while retaining the 'simple' structure of hydrogen jet flames.

Experimental observations show that the squared-off nozzle stabilizes the flame thus avoiding a pilot [3]. Although not experimentally proved, but shown by the present numerical simulations, the anchoring is likely to be due to a small recirculation zone produced by the bluff-body. Simultaneous Raman/Rayleigh/LIF measurements of temperature and concentrations, and three-component LDV velocity data are provided by the experimentalists. Measurements for both velocity and scalars (including minor species such as OH) of the same flame are also provided: they are important to understand interactions between fluid dynamics and chemical kinetics. However, the first measurement station is at 45.8 mm from the injector. Hence, although according to experimentalists the actual flame seems to be continuous and not experiencing any lift off or localized extinction, nothing can be stated precisely about flame dynamics at shorter distance from the inlet.

In this article, unsteady numerical simulation of the 'Flame A' are performed using the Fractal Model (FM) [4–6] as subgrid closure for Large Eddy Simulation. However, it is observed that for present simulations a three-dimensional axisymmetric formulation, thus formally two-dimensional, is used; therefore, it is preferable to talk of unsteady simulation rather than LES. The aim is to analyse the mentioned issue of flame anchoring and the effects of some modelling parameters, such as boundary conditions and chemical mechanisms. In a nutshell, present simulations represent two-dimensional preliminary tests aimed at providing some guidelines for a future fully three-dimensional Large Eddy Simulation of the same burner.

2. Numerical simulation set-up

Numerical simulations are performed by means of the in-house code HeaRT (Heat Release and Turbulence) using parallel computers available at the ENEA computational grid [7]. For the present work explicit finite differences (convective and viscous CFL are 0.1 and 0.3, respectively), second order accurate in space (centred) and third order (Runge–Kutta) in time are used to solve the fully compressible Navier–Stokes equations in a cylindrical coordinate system. Explicit (nonlinear) filtering of field variables is adopted to reduce numerical oscillations due to the centred spatial scheme [8], thus avoiding the requirement for a staggered grid. The perfect gas law is assumed as state equation. The computational domain is cylindrical and includes two inlet zones for fuel and air channels extending 5 mm upstream of the inlet sections. The computational grids are structured.

2.1. *Turbulent combustion closure*

The unsteady simulations performed are based on the Fractal Model, FM, for the details of which the reader is addressed to previous reference works [4–6].

FM is an 'eddy viscosity' subgrid model, turning itself off in the laminar regions of the flow. The self-similar turbulent energy/vortex cascade, from the local filter size Δ down to the local dissipative scale η, is modelled in each computational cell by means of a fractal (recursive) technique, i.e.

$$\frac{E_\Delta}{\tau_\Delta} \approx N_\eta \cdot \frac{E_\eta}{\tau_\eta} \longrightarrow \frac{u_\Delta^3}{\Delta} \approx N_\eta \cdot \nu_\eta \frac{u_\eta^2}{\eta^2}, \tag{1}$$

where E is the energy per unit mass, τ_Δ the eddy turnover time at scale Δ ($\approx \Delta/U_\Delta$, U_Δ being the velocity at scale Δ), N_η the number of dissipative scales η locally generated, τ_η the dissipative time ($\tau_\eta = \eta^2/\nu_\eta$), and ν_η the kinematic viscosity at scale η. Details about estimating N_η are given in [5]. Based on this cascade the scale η is estimated as [6]

$$\eta = N_\eta^{1/4} \cdot \left(\frac{\nu_\eta}{\nu_\Delta}\right)^{3/4} \cdot \frac{\Delta}{Re_\Delta^{3/4}}. \tag{2}$$

The subscripts Δ and η represent the filtered values in the cell and those related to the dissipative subgrid scales, respectively. It is observed that in reacting zones ν_Δ and ν_η differ since chemical reactions are assumed to take place at the scale η, and thus the state of these scales will be different from the 'filtered' state of the cell. The term $(\nu_\eta/\nu_\Delta)^{3/4}$ can be of order 10.

Equation (2) indicates that η grows with increasing temperature. The FM adapts itself to local flow conditions. In regions where $\Delta/\eta = 1$ the local spatial filter Δ equals the dissipative scale, which can be resolved without any modelling (the FM turns itself off). This typically happens in the hottest flow regions.

Wherever $\Delta/\eta > 1$, the FM models subgrid turbulent stresses by means of an 'eddy viscosity' μ_t [4],

$$\mu_t = \sigma_{\mathrm{FM}} \cdot \pi^{-1} \cdot \mu_\Delta \cdot \left[\left(\frac{\Delta}{\eta}\right)^2 - 1\right], \tag{3}$$

which yields automatically $\mu_t = 0$ when $\Delta/\eta = 1$ (in laminar regions, and in particular near walls). In this expression σ_{FM} is the sole 'calibration constant' of the model; previous comparisons with subsonic combustion experiments suggest values in the range 0.1–0.6 [4, 5, 9, 10]. This parameter can also be dynamically adjusted [11].

Combustion chemistry close to dissipation scales is treated by the FM by means of a Perfectly Stirred Reactor (PSR), with a residence time assumed equal to the local 'eddy turnover time' τ^* of the dissipative scales (this idea goes back to the Eddy Dissipation Concept [12]). The volume fraction γ^* occupied by the dissipative structures in each computational cell is estimated by means of the local filter Δ (i.e. the size of the fractal seed), the local dissipative scale η (i.e. the fractal measurement unit) and the local fractal dimension D_3:

$$\gamma^* \propto \left(\frac{\Delta}{\eta}\right)^{D_3-3}. \tag{4}$$

The fractal dimension is given by $D_3 = 1 + \ln N_\eta / \ln(\Delta/\eta)$. More details about γ^* and D_3 estimation are provided in [4, 6].

Once the volume fraction of the reacting 'fine structures' is known, the local chemical heat release is naturally modelled as a subgrid effect founding on the EDC model [12]. The Favre filtered source terms are $\widetilde{\omega}_i = \gamma^* \omega_i^*$ in the N species equations, and $\widetilde{\dot{Q}} = \sum_{i=1}^{N_s} \gamma^* \omega_i^* \widetilde{\mathcal{H}}_i$ in the energy equation where $\widetilde{\mathcal{H}}_i$ is the filtered total enthalpy of the i-th species, the sum of the sensible and formation enthalpies. The instantaneous production/destruction rate of the species i inside the reactor, ω_i^*, is given by the Arrhenius expressions of the particular chemical mechanism adopted. ω_i^* depends on the state of the reactor, defined by its concentrations Y_i^*, temperature T^* and pressure p^*. These are estimated assuming that during each time step:

i the pressure p^* is constant and equal to the filtered pressure $\overline{p}$ in the cell;
ii the reactants are perfectly mixed inside the reactor, whose mass is constant;
iii the local 'fine structures' are modelled as a steady and adiabatic Perfectly Stirred Reactor;
iv the characteristic time of the subgrid reactor is equal to the 'eddy turnover time' of the dissipative vortices η [5].

With the previous assumptions, species and energy balance equations written for this subgrid PSR reactor are solved at each computational cell to obtain T^* and Y_i^*.

Where $\Delta/\eta \leq 1$ the local scale Δ is dissipative; no modelling is required, $\gamma^* = 1$ and the local filtered and subgrid quantities coincide.

Subgrid turbulent thermal conductivity is estimated as $K_t = (\mu_t/\mu)$ K; subgrid turbulent diffusivity by means of an assumed constant turbulent Schmidt number, i.e. as $D_t = \nu_t / Sc_t$ (with $Sc_t = 0.7$). These subgrid quantities are added to the molecular ones.

2.2. *Molecular properties*

Molecular transport mechanisms not taken into account in the resolved equations are: the Dufour and Soret effects, cross-diffusion, pressure gradient diffusion, and diffusion by means of the body force. Preferential diffusion is considered and the species diffusive mass flux is modelled by means of the Hirschfelder–Curtiss law.

All molecular properties for individual chemical species, except their binary mass diffusivities, are calculated a priori by using the software library provided by A. Ern (EGlib) [13, 14]. In particular, kinetic theory is used for dynamic viscosity [15, p. 23–29] and thermal conductivity [15, p. 274–278]. The calculated values are stored in a look-up table from 200 to 5000 K every 100 K. Values for intermediate temperatures are calculated at run-time by linear interpolation. Binary mass diffusion coefficients are calculated by means of kinetic theory expressions [15, p. 525–528] at run-time.

The mixture-average properties are estimated at run-time. In particular, the simulations used in this work for comparison with experimental data implement a simple and crude mass-weighted mixing law for both viscosity and thermal conductivity (e.g. $\mu = \sum_{i=1}^{N_s} Y_i \mu_i$). The Hirschfelder–Curtiss approximation is instead adopted for the effective diffusion coefficient, $D_{i,\mathrm{mix}}$, of species i into the rest of mixture [15, p. 258] [16, 17]. In this way, as discussed in Section 4.1.1, preferential diffusion of individual species is taken into account. A review of the calculation of molecular properties, especially focused on diffusion coefficients, can be found in [18].

Mass-weighted average expressions for mixture molecular properties (such as the ones used in the present work for viscosity and thermal conductivity) are commonly adopted in CFD calculations due to their simplicity and low cost. More accurate and computationally expensive formulations exist and they may strongly affect results. For example, it is known that incorrect

diffusivities imply incorrect estimation of the peak dissipation rate and the maximum reaction rate. In fact, in [19, p. 88–89], numerical results show that accurate treatment of differential diffusion can be just as important as accurate modelling of chemical kinetics. Hence, future three-dimensional LES simulations of the same flame will be done by using more accurate expressions for viscosity and thermal conductivity.

2.3. *Chemical kinetics*

From the point of view of chemistry, two different types of chemical mechanisms are considered. In the first one, named FAST, a hybrid fast-chemistry-single-step approach is assumed. In the second one, named RED, a finite rate approach is used.

In the simplified FAST case, only two reactions are considered:

$$\mathrm{H_2} + \frac{1}{2}\mathrm{O_2} \rightarrow \mathrm{H_2O} \tag{5}$$

$$\mathrm{CO} + \frac{1}{2}\mathrm{O_2} \leftrightarrow \mathrm{CO_2}. \tag{6}$$

Comparing the oxidation kinetics of H_2 and CO [20, pp. 133–137], [21, Ch. 4], [22, pp. 72–76], it is observed that CO has slower kinetics. This issue is taken into account by using two different approaches for the two reactions: a fast-chemistry approach for the first one, and a single-step reversible mechanism for the second one. Based on previous experience [23, pp. 64–77], it is observed that assuming a fast-chemistry approach for both reactions generally produce worse predictions.

Hence, the reaction rate of the first reaction is modelled according to the fast-chemistry approach of the Eddy Dissipation Concept [12], i.e.

$$\omega^*_{\mathrm{H_2}} = -\frac{\rho^*}{\tau^*(1-\gamma^*)} \min\left[Y^*_{\mathrm{H_2}}, \frac{Y^*_{\mathrm{O_2}}}{8}\right], \tag{7}$$

where γ^* and τ^* are the fraction of reacting volume and a characteristic residence time, respectively, and Y^*_i are mass fractions. These quantities are specified within the subgrid model FM used in present simulations. Instead, the reaction rate of the second reaction is modelled according to a single-step reversible mechanism [24] derived from that of Dryer and Glassman [25]. In particular, the forward and backward rates are given by (in terms of molar concentrations)

$$\omega^*_{\mathrm{CO}} = -k_f\,[\mathrm{CO}]^*\,[\mathrm{H_2O}]^{*\,0.5}\,[\mathrm{O_2}]^{*\,0.25} \tag{8}$$

$$\omega^*_{\mathrm{CO_2}} = -k_b\,[\mathrm{CO_2}]^*. \tag{9}$$

The reaction constants are in the Arrhenius form, $k_{f,b} = A_{f,b}\exp\left[-\mathrm{E_a}/(\Re_\mathrm{u}\mathrm{T})\right]$, with the constants reported in Table 1. From Equation (8) it is noted that the CO reaction does not start without an initial H_2O concentration. However, the complete scheme adopted in the FAST case is self-starting, because the oxidation of H_2 is infinitely fast and generates the H_2O needed to oxidize CO.

It is observed that making use of a fast-chemistry approach is an easy way to numerically ignite a mixture and produce an initial flame, thus avoiding problems relative to the choice of the right location of artificial 'hot spots'. However, it is well known that a fast-chemistry approach, or a single step mechanism, predicts generally well the flame speed in a wide range of operative

Table 1. CO oxidation parameters associated to Equations (8) and (9), as proposed in [24, 25]. Units are in m^3, kmol, s, K, kcal.

Parameter	$T^* < 1150$ K	$T^* > 1150$ K
A_f	$2.61 \cdot 10^{12}$	$6.52 \cdot 10^6$
E_{a_f}	45 566	15 968
A_b	$5.00 \cdot 10^8$	$5.00 \cdot 10^8$
E_{a_b}	39 990	39 990

conditions, but has also many defects, critical in certain applications. For instance, assuming that the only products are CO_2 and H_2O, temperatures are typically overestimated. At adiabatic flame temperature conditions typical of hydrocarbon/air combustion, ~ 2000 K, a non-negligible quantity of CO and H_2 exists in equilibrium with CO_2 and H_2O. Moreover, this is true also for other (radical) species, such as H, O and OH, even if their concentrations are much smaller. These radicals are formed by endothermic reactions, lowering the local temperature below that predicted by a single step mechanism. Hence, once a reacting flowfield has been obtained with this simple chemistry, it is suggested to improve results by using a more complex chemical mechanism taking the previous flowfield as initial condition.

In the RED cases instead, a finite-rate chemistry is adopted. In particular, the six-step-ten-species reduced mechanism of Chen [2] (based on a skeletal mechanism of 70 reactions with five species assumed in partial equilibrium), including main radical species, is assumed:

$$O_2 + H \leftrightarrow OH + O \tag{10}$$

$$H_2 + O \leftrightarrow H + OH \tag{11}$$

$$H_2 + OH \leftrightarrow H + H_2O \tag{12}$$

$$H_2 \leftrightarrow 2H \tag{13}$$

$$CO + OH \leftrightarrow H + CO_2 \tag{14}$$

$$N_2 + O_2 \leftrightarrow 2NO. \tag{15}$$

The reaction rates of this reduced mechanism are defined as linear combinations of reaction rates of the skeletal mechanism. Chemical data and details of this reduced mechanism are not reported in this work for brevity: the whole mechanism of Chen can be freely downloaded from [2, in the 'Computational Submodels', 'Chemical Mechanisms', 'Chemistry', '$CO/H_2/N_2$' section]. It is observed that the Chen chemical mechanism is not self-starting, i.e. high temperature alone is not sufficient to activate reactions; also a non-zero distribution of some radical species must be prescribed to ignite the mixture.

With the hydrogen fast-chemistry assumption the flame is obviously anchored. Instead, in the finite-rate case, if the spatial resolution in the near-nozzle region is not so high to reveal the fluid dynamic and chemical details of anchoring, the flame blows-off. Since the computational grid is structured, the number of grid nodes needed to simulate the whole flame becomes high, especially looking to future three-dimensional LES simulations. Therefore, to simulate this flame on a coarse grid (to keep the computational cost low) with realistic kinetics it is necessary to develop an artificial stabilization mechanism that produces effects similar to the actual one. This is done by analysing results obtained in a small computational domain close to injection and with a very fine grid (RED_{ZOOM} case in the following).

2.4. *Boundary conditions*

When no explicit boundary conditions fix the dependent variables, but the numerical implementation requires us to specify something, the conservation equations themselves can be used to provide physical boundary conditions.

It is well known that the Navier–Stokes equations are not hyperbolic since the viscous terms increase the order of the system and change its mathematical nature. However, Navier–Stokes equations propagate waves like Euler equations do. Hence, Euler boundary conditions appear as first-order candidates to treat Navier–Stokes boundary conditions. In a first approximation, it is logical to associate the waves involved in the Navier–Stokes equations only to the hyperbolic part of them. In a nutshell, these waves can be identified by the same procedure as for Euler equations, thus neglecting waves associated to diffusion processes. It was demonstrated that this assumption is justified for high Reynolds number flows as well as for very viscous flows [26]. Once these waves have been analytically calculated in terms of their amplitude L_i and characteristic velocities, the Navier–Stokes equations can be recast in terms of these quantities and used at boundaries to specify physical boundary conditions for some dependent variables. The waves moving towards the boundary from inside the calculation domain (named 'outgoing waves') can be computed using information about the inner field. Instead, waves coming from the space outside the computational domain (named 'incoming waves') must be specified. Especially when acoustic waves are involved in the simulations, it is very important to avoid or at least reduce numerical reflections of outgoing waves at open boundaries to avoid unphysical oscillations in the flowfield. To this end, non-reflecting and partially non-reflecting boundary conditions are used [26, 27].

According to characteristics analysis the amplitude of waves involved in the Navier–Stokes system (here specialized at a generic boundary normal to the z-direction) can be written as:

$$\begin{aligned}
L_1 &= (U_z - a)\left(\frac{\partial p}{\partial z} - \rho a \frac{\partial U_z}{\partial z}\right) \\
L_2 &= U_z\left(a^2 \frac{\partial \rho}{\partial z} - \frac{\partial p}{\partial z}\right) \\
L_3 &= U_z \frac{\partial U_r}{\partial z} \\
L_4 &= U_z \frac{\partial U_\vartheta}{\partial z} \\
L_5 &= (U_z + a)\left(\frac{\partial p}{\partial z} + \rho a \frac{\partial U_z}{\partial z}\right).
\end{aligned} \tag{16}$$

In particular, the outflow plane normal to the jet flow is assumed non-reflecting: therefore, the amplitude of the incoming wave into the computational domain is forced to be nil, i.e. $L_1 = 0$, while the amplitude of the outgoing waves is estimated from the computational field. All variables are obtained from their transport equations written in their characteristics form, except for chemical species, for which a nil gradient condition is applied. Pressure comes out from the equation of state.

At the inlet, species are specified. Density, velocity and temperature are computed by solving continuity, momentum and energy equations in their characteristics form; the amplitudes of the incoming waves associated to velocity components and temperature are modelled by means of a

relaxation method [27]:

$$L_2 = U_z \left(\frac{\gamma - 1}{\gamma} a^2 \frac{\partial \rho}{\partial z} - \rho R_g \frac{\partial T}{\partial z} \right) \rightarrow \tag{17}$$

$$L_2 = -\sigma_{\mathrm{INLET}} U_z \rho R_g \frac{T - T_\infty}{L_{\mathrm{in}}}$$

$$L_3 = \sigma_{\mathrm{INLET}} U_z \frac{U_r - U_{r_\infty}}{L_{\mathrm{in}}} \tag{18}$$

$$L_4 = \sigma_{\mathrm{INLET}} U_z \frac{U_\theta - U_{\theta\infty}}{L_{\mathrm{in}}} \tag{19}$$

$$L_5 = \sigma_{\mathrm{INLET}} \rho a^2 \frac{U_z - U_{z_\infty}}{L_{\mathrm{in}}}. \tag{20}$$

Here, $T_\infty = 292\,\mathrm{K}$, $U_{z_\infty} = 76\,\mathrm{m\,s^{-1}}$ and $U_{r_\infty} = U_{\theta_\infty} = 0$ are the quantities upstream of the fuel inlet boundary towards which the calculated quantities at the fuel inlet relax and σ_{INLET} is a relaxation constant. This means that inlet boundary conditions are partially non-reflecting. Pressure is obtained by means of the perfect gas law.

On the lateral surface (here called CLOAK and located at $r_{\max}$) of the cylindrical domain species are obtained by means of a simple nil gradient condition. Density, velocity and temperature are calculated by solving continuity, momentum and energy equations in their characteristics form. Pressure is obtained by means of the perfect gas law. A pressure relaxation model, i.e.

$$L_1 = (U_z - a) \left(\frac{\partial p}{\partial z} - \rho a \frac{\partial U_z}{\partial z} \right) \rightarrow L_1 = \sigma_{\mathrm{CLOAK}} \left(1 - M^2\right) a \frac{p - p_\infty}{r_{\max}} \tag{21}$$

is assumed for the amplitude of the incoming acoustic wave. Furthermore, in simulations involving the reduced chemical mechanism of Chen ($\mathrm{RED}_{A,B,C}$ in the following), a linear distribution of target pressures along the 'CLOAK' is assumed. In particular, $p_\infty = 1\,\mathrm{atm}$ is imposed at the exit with a difference of 100 Pa between the inlet and the outlet target values; this gap 'anchors' the motion of the coaxial air jet in the appropriate direction. The pressure difference of 100 Pa was determined empirically based on preliminary tests and checking that it did not produce an acceleration of the coaxial air not present in the actual flow. It is noted that this 'trick' to stabilize the boundary conditions on the CLOAK boundary could be avoided by widening the computational domain to include more of the surrounding atmosphere, but inevitably increasing the computational cost.

It is not trivial to observe that partially non-reflecting boundary conditions are needed instead of purely non-reflecting ones to impose boundary conditions to variables in terms of their values (pressure at the open boundary, velocity and temperature at the inlet). The value of the constants σ_{CLOAK} and σ_{INLET} used in the relaxation models should be close to zero to 'avoid' numerical reflections, but not so much to avoid drift of the associated variables during the computation. In particular, it is well known that if the relaxation constant for the pressure at the CLOAK boundary was nil or very small, pressure would decrease during simulations. This is not critical for short runs but leads to numerical problems and unphysical results over long runs, especially for reacting flows.

3. Strategy of the present study

Different simulations, whose characteristics are reported in Table 2, are performed to check the effects of some modelling constants on results and, especially, the effects of grid spatial resolution and chemistry on the flame stabilization mechanism. This issue is the main concern for the numerical simulation of the present flame. In fact, it is likely anchored by means of a small recirculation zone due to the wall of the nozzle tubing, thus avoiding the use of a pilot flame. This experimental convenience may lead to computational inconvenience, in particular when structured grids are used, as in present simulations. The thickness of the tubing is 0.88 mm and the spatial resolution required to capture the details of the near-nozzle flow is very high. This work shows that these details are important to stabilize the flame.

With respect to spatial resolution, two types of simulations are performed: one to investigate the whole flame (cases FAST, RED_A, RED_B, RED_C) and the other (case $\mathrm{RED}_{\mathrm{ZOOM}}$), on a smaller computational domain with a much finer grid, to focus on the stabilization mechanism close to the injection region. Concerning chemical kinetics, two types of simulations are conducted: one with a very simplified chemistry (case FAST), and the other with a reduced mechanism including main radical species (cases RED).

The influence on the results of some modelling constants, i.e. the relaxation constant σ_{CLOAK} and the subgrid model constant σ_{FM}, is also checked.

It was observed [27] that relaxation constants in partially non-reflecting boundary conditions control the cut-off frequency of the outgoing wave below which numerical reflection takes place. In fact, a boundary relaxation time can be defined, e.g. as $\tau_{\mathrm{CLOAK}} = 2r_{\max}/(\sigma_{\mathrm{CLOAK}}\, a)$, a being the sound speed (340 m/s for air and 524 m/s for syngas, at their inlet temperature). Values of relaxation constants, the associated times and cut-off frequencies used in the present simulations, are listed in Table 2. In particular, σ_{CLOAK} for the $\mathrm{RED}_{A,B,C}$ simulations are chosen to have the same cut-off frequency. Since the $\mathrm{RED}_{\mathrm{ZOOM}}$ simulation is focused on the stabilization and the convective time is small, a smaller σ_{CLOAK} is assumed to reduce numerical reflection; pressure drift is negligible in the small time window simulated. The pressure difference of 100 Pa between the inlet and outlet target pressures on the lateral boundary (CLOAK), imposed for the RED cases, is not adopted for the $\mathrm{RED}_{\mathrm{ZOOM}}$ simulation.

Considering the RED_A and RED_B cases it is possible to check the effect of the subgrid model constant σ_{FM}. It is observed that increasing σ_{FM} the diffusion, and in particular the radial diffusion, increases. Hence, the flame in case RED_B is expected to be closer to the lateral open boundary (as also confirmed by numerical results) and the 'numerical' interaction between the boundary condition and the inner flow dynamics is expected to increase. To check possible effects of this interaction, i.e. to check the effect of the lateral boundary condition (CLOAK) distance ($r_{\max}$) from the axis of the burner, $r_{\max}$ is increased in the RED_C simulation.

4. Results

Results are first obtained with a coarse grid and assuming a fast-chemistry approach for hydrogen oxidation and a single step mechanism for carbon monoxide oxidation (FAST case). The main aim of this simulation is to provide an initial flowfield for the RED simulations that adopt a more complex chemical mechanism (six-step-ten-species), including main radical species. The fast-chemistry approach makes ignition of reactants easier to realize than using artificial 'hot spots', that must be opportunely located and that can be sources of numerical instabilities during the ignition transient.

However, with the six-step mechanism and the same computational grid as the FAST case, the flame blows off. This means that the fluid dynamic details of flame anchoring in the bluff-body

Table 2. Computational nodes in the cases simulated and values assumed for the constants of the SGS model and for the relaxation models at partially non-reflecting boundary conditions. Note that the computational domain has three zones, two for the inlets of fuel and air, extending 5 mm upstream of the nozzle exit, and the third one (referred to as FZ, i.e. Flame Zone) for the main combusting zone.

CASE	FAST	$\mathrm{RED}_{\mathrm{ZOOM}}$	RED_A	RED_B	RED_C
$r_{\max}$ [cm]	10	1.5	4.58	4.58	10
$z_{\max}$[cm] in FZ	38	2	78.45	78.45	78.45
r nodes in FZ	76	461	71	71	95
z nodes in FZ	302	291	648	648	648
Total nodes	24047	206349	47900	47900	63452
σ_{FM}	0.35	0.1	0.2	0.35	0.35
σ_{INLET}	–	0.1	0.1	0.1	0.1
τ_{INLET} [ms]	–	0.19	0.19	0.19	0.19
f_{INLET} [Hz]	–	5240	5240	5240	5240
σ_{CLOAK}	0.3	0.01	0.08	0.08	0.175
τ_{CLOAK} [ms]	1.96	8.82	3.37	3.37	3.37
f_{CLOAK} [Hz]	510	113	297	297	297

region are not captured at all. This quite unexpected result suggests we analyse the anchoring mechanism for this flame in more detail. Hence, a simulation is performed with increased spatial resolution onto a small region close to the injector ($\mathrm{RED}_{\mathrm{ZOOM}}$ case) with the aim of investigating the physical phenomena that cause a stable and continuous ignition of the reactants as in the experiment. These results are also used to develop an artificial stabilization mechanism to simulate the whole flame with a coarser computational grid ($\mathrm{RED}_{A,B,C}$ cases).

The RED_C numerical results will be shown to have the best agreement with experimental data. For this reason, after the analysis of the $\mathrm{RED}_{\mathrm{ZOOM}}$ results, only the RED_C simulation, among the $\mathrm{RED}_{A,B,C}$ cases, will be used to describe the flame characteristics.

4.1. *Analysis of the flame anchoring*

To understand the actual flame stabilization only a small region, 25×15 mm (axial and radial sizes, respectively), is simulated with a very fine grid (10^{-5} m spatial resolution close to the nozzle) in the $\mathrm{RED}_{\mathrm{ZOOM}}$ case. Since Δ, the local characteristic size of the filter, is very small, the ratio Δ/η is small too ($\sim$3.2, η being the dissipative scale estimated by means of the fuel jet Reynolds number and its diameter assumed as the integral macroscale). It is stressed that this ratio is even smaller in the hot regions due to the increase of viscosity, but is far from DNS resolution in the high speed cold regions (it is observed that the maximum velocity of the fuel jet at its exit is much higher than its bulk velocity, i.e. $\sim$104 m s^{-1} versus 76 m s^{-1}). Hence, the SGS eddy viscosity is supposed to vanish or at least to have an order of magnitude comparable to or less than that of the molecular viscosity in the low velocity or high temperature regions. This issue was checked and verified: the eddy viscosity is a maximum of the order of 10^{-4} kg m^{-1} s^{-1} in the high speed regions of the cold fuel jet, and reaches lower values in the other zones, down to order 10^{-7} kg m^{-1} s^{-1} in the recirculation immediately downstream of the bluff-body. Consequently, the $\mathrm{RED}_{\mathrm{ZOOM}}$ simulation is a 'rough DNS' performed with a centred second order accurate spatial scheme. If the centred second order DNS (even though this simulation does not claim to be a DNS) could arise some perplexity due to the low numerical accuracy of the spatial integration, it is observed that the second order centred scheme was proved to be sufficiently accurate to perform DNS in turbulent channel flows [28, 29] and in turbulent non-premixed flames [30].

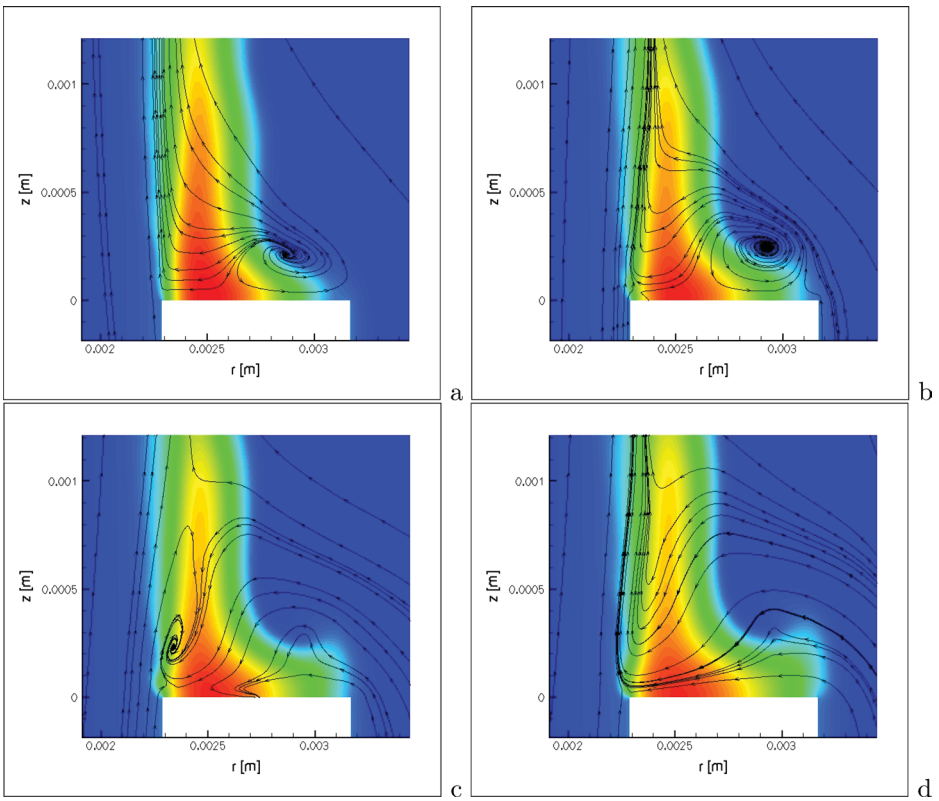

Figure 1. Temperature contours, details of the shedding and flame anchoring predicted in the RED_{ZOOM} simulation. The delay time between each frame is $\sim 30\,\mu$s.

Results show a well anchored flame front and seem to confirm what was expected by experimentalists, i.e. that the flame is stabilized by a small recirculation zone due to the fuel pipe wall thickness. In fact, as shown in Figure 1, the end of the injection pipe works as a bluff-body to anchor the flame. In particular, the flame is continuously attached at the inner edge, despite the alternate shedding of vortices from the inner and outer edges at $\sim$11 kHz that cause roll-up of the flame front more downstream. These vortices enhance mixing and anchor the flame. The time-averaged flowfield reported in Figure 2(a) shows a recirculation skewed towards the outer edge. This is due to the longer residence time of the outer vortex that brings some coaxial air towards the fuel jet and produce an averaged flame front attached to the inner edge. The strong stability of this 'hot spot' close to the injector is also confirmed by the low rms temperature fluctuations in that region (see Figure 2b).

In this work an adiabatic condition was applied at the walls. This type of thermal condition may have negative effects on 'numerical' flame anchoring. In fact, if the temperature decreases quickly at some flow-points adjacent to the walls, also the wall-points close to those flow-points will experience the same temperature decrease instantaneously. The inertia of the solid wall in maintaining its heat is practically nil; hence, the wall is unable to heat reactants and to favour flame stability. In difficult anchoring conditions, such as the present one, this can be critical. Despite this potential problem, the flame is well anchored on the inner edge of the fuel pipe in numerical simulations.

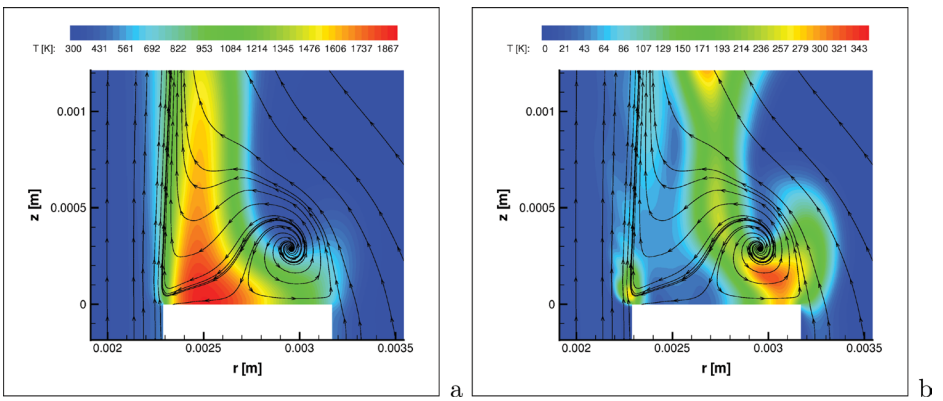

Figure 2. Averaged (a) and rms (b) temperature contour map predicted in the $\mathrm{RED}_{\mathrm{ZOOM}}$ simulation. The averaged streamlines are also shown in both pictures, showing an averaged recirculation zone skewed towards the outer edge of the bluff-body.

To better understand the actual flame stabilization and discover the physical mechanisms mainly responsible for the anchoring, the characteristic times of the physics involved in the simulation are analysed. Assuming the local filter size Δ (given by the cube root of the computational cell volume) as the characteristic length, the following times are defined and calculated:

- convective time of fluid motion, $\tau_{\mathrm{conv}} = \Delta/U$, U being the local filtered velocity module;
- momentum diffusion time, $\tau_\nu = \Delta^2/\nu$, ν being the local filtered kinematic viscosity;
- acoustic time, $\tau_a = \Delta/a$, a being the local filtered sound speed;
- heat diffusion time, $\tau_\alpha = \Delta^2/\alpha$, α being the local filtered thermal diffusivity;
- preferential H_2 mass diffusion time, $\tau_{D_{H_2}} = \Delta^2/D_{H_2}$, D_{H_2} being the H_2 diffusion coefficient;
- chemical production time of radicals H, O, OH, and of H_2O, $\tau_i = \rho Y_i/\omega_i$, ρ, Y_i and ω_i being the local filtered density, mass fraction of the chemical species considered, and their production rate, respectively.
- heat release time, $\tau_{\Delta H_R} = \Delta H_R/(\rho h_{\mathrm{sens}})$, $\Delta H_R = \sum_{i=1}^{N_s} \omega_i \mathcal{H}_i$ being the heat of reaction, and $\mathcal{H}_i$ the total enthalpy, sum of sensible, h_{sens_i}, and formation enthalpies.

It is observed that the turbulent transport properties are used in calculating these times, but they are very close to their molecular value since the eddy viscosity is negligible due to the high spatial resolution. These characteristic times are calculated in two small regions marked in Figure 3(a) with yellow (closer to the bluff-body) and purple boxes at the two different instantaneous fields shown in Figure 1(a) and (c), that correspond to opposite phases of the vortex shedding (denoted as instants 1 and 2 in the following). The size of the lower box is chosen in order to include the maximum extension of the recirculation in Figure 1(c).

Looking at the characteristic times versus temperature distributions in Figure 3 it is first noted that acoustic time scales (of the order of 10^{-7} s) are well separated from other physical time scales. Hence, the interaction between acoustics, fluid dynamics and combustion is not present in this flame (at least in this computational domain). The dissipative time scales (important in determining eddy lifetime) in the region close to the injection does not change significantly switching from instant 1 to instant 2 (see Figures 3b and 3c), while it changes moving towards shorter time scales in the higher subregion (see Figure 3d); this is in agreement with temperature dynamics (average and rms fluctuation) shown in Figure 2, since kinematic viscosity strongly depends on temperature.

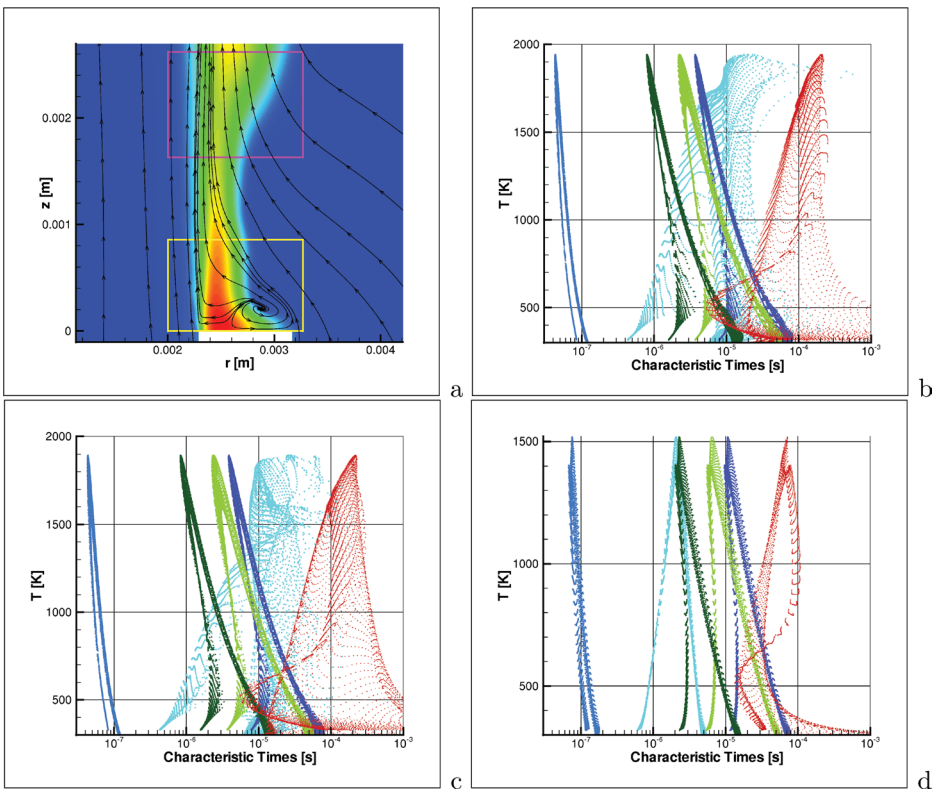

Figure 3. Characteristic times versus temperature distributions obtained in the RED_{ZOOM} simulation by considering the two subzones shown in (a) using the instantaneous field shown in Figure 1(a) just as an example. The characteristic times, whose definitions are given in the text, are associated to the following phenomena: convection (heaven), viscous dissipation (dark blue), acoustics (light blue), heat diffusion (light green), preferential H_2 mass diffusion (dark green), and heat release (red). The distributions associated to the lower (marked yellow) zone of the instantaneous fields shown in Figures 1(a) and (c) are in (b) and (c), respectively; those associated to the higher (marked purple) zone of the instantaneous field shown in Figure 1(a) are in (d).

Comparing Figures 3(b) and (c), it is possible to see the effects of opposite phases of the vortex shedding on distributions inside the box closer to the injector (the yellow one). The main effect is that the distribution of the convective times of fluid motion (heaven) is shifted towards slower time scales in the high temperature region of the instant 2 with respect to instant 1. This is due to the presence of the vortex where the flame is located in instant 2 (see Figure 1c). Especially in this configuration the flame anchoring is supposed to be favoured by the shorter time scales associated to preferential H_2 mass diffusion and to heat diffusion that enhance mixing and preheating of reactants.

Comparing Figures 3(b) and (d), which refer to the lower and upper boxes, respectively, of the same instantaneous field shown in Figures 1(a) and 3(a), it is observed that when recirculation is not present (upper box, Figure 3d) convective time scales become shorter and compete with stabilizing mechanisms, such as the preferential H_2 mass diffusion.

Hence, from these distributions it can be deduced that the competing phenomena in the flame anchoring mechanism for the RED_{ZOOM} simulation are convection of fluid motion, heat diffusion and H_2 preferential diffusion. The fact that the heat release time is slower than the convective time

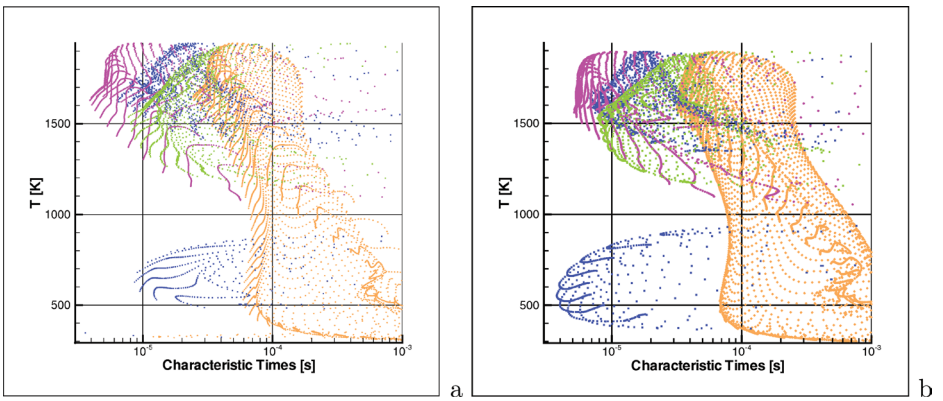

Figure 4. Chemical production times versus temperature distributions obtained in the $\mathrm{RED}_{\mathrm{ZOOM}}$ simulation by considering the subzone closer to the injection region, shown in Figure 3(a), and using the instantaneous fields shown in Figure 1(a), (a), and Figure 1(c), (b). The characteristic times, whose definitions are given in the text, are associated to the following species: H (purple), OH (blue), O (green), and H_2O (orange).

seems not to be so important in anchoring. This issue, curious at first glance, can be explained by considering the flame propagation speed that can be locally defined (since where the flame develops there is a reacting mixture) even though the flame is macroscopically non-premixed. It is known that the laminar flame speed depends not only on the reaction heat ΔH_R, but also on the thermal diffusivity, α, and diffusion coefficients, D_i [32, pp. 164–170]. Based on the chain branching theory [32, p. 170], the local laminar flame speed can be estimated with good accuracy taking into account the slower radical dynamics in terms of its diffusion, production rate and concentration, i.e. $S_L = 2D_i\omega_i/(\rho Y_i)$. The validity of this expression was verified by simulating stoichiometric freely propagating syngas–air flames by means of the CHEMKIN code. Analysing chemical production time distributions of some species shown in Figure 4, it is observed that time scales of radical species are shorter than stable products, such as water. Furthermore, it is

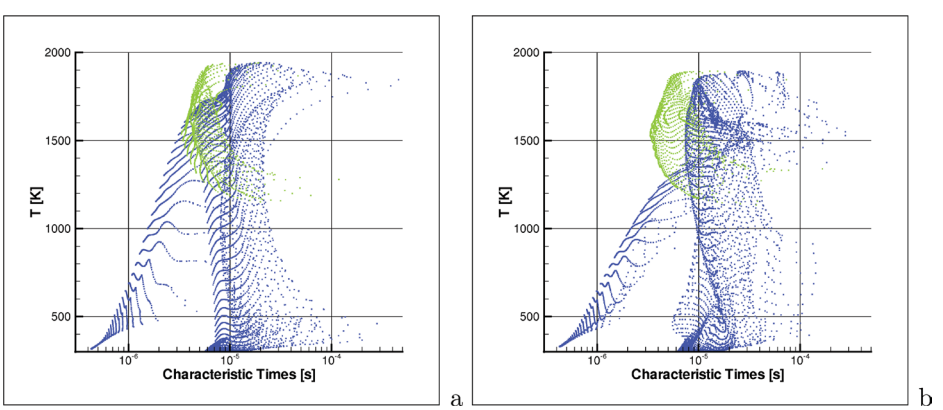

Figure 5. Characteristic times versus temperature distributions for convection of fluid motion, τ_{conv} (blue), and flame propagation, τ_{S_L} (green). Data refer to the $\mathrm{RED}_{\mathrm{ZOOM}}$ instantaneous fields shown in Figure 1(a), (a), and Figure 1(c), (b), and are extracted from the subzone closer to the injection region, shown in Figure 3(a).

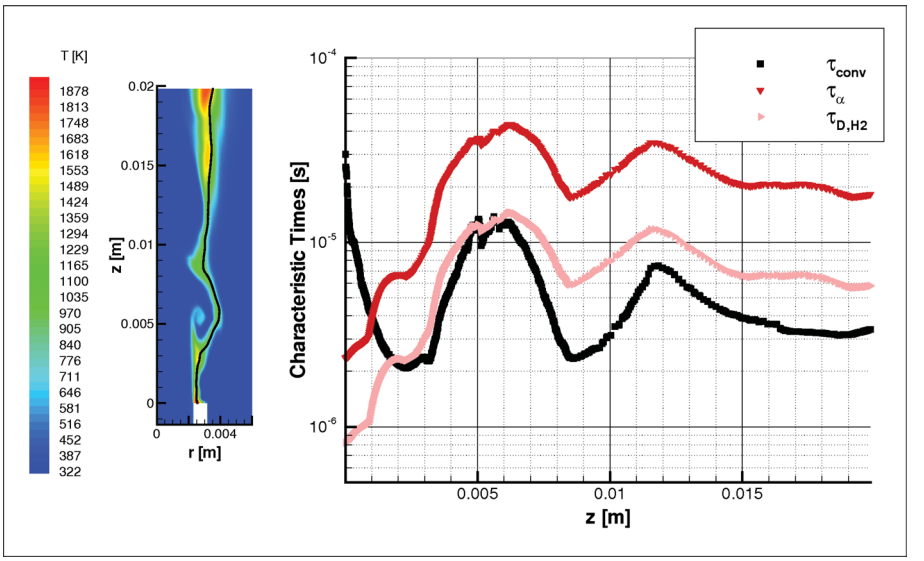

Figure 6. The competing phenomena in the flame anchoring mechanism as deduced from for the RED_{ZOOM} simulation are fluid dynamic convection (black, lower curve), heat diffusion (red, upper curve) and hydrogen preferential diffusion (pink, middle curve). Their characteristic times are here reported for the instantaneous field shown in Figure 1(a). In particular, these times are sampled along the stoichiometric Bilger mixture fraction [31] iso-line (drawn in black in the flowfield on the left), $F_{\text{BLGR}} = 0.295$, and plotted versus the axial coordinate, z.

noted that the radical H is generally the fastest among the radical species involved in the present study. Distributions of convective time scales of fluid motion, τ_{conv}, and of flame propagation time scales, $\tau_{S_L} = \Delta / S_L$, extracted from the subzone closer to the injection region where the flame is anchored are shown in Figure 5 for instants 1 and 2. These time scales being comparable in the high temperature region, the existence of a stably anchored flame can be easily deduced. In a nutshell, the local flame propagation speed can be used as a synthetic quantity of flame anchoring since it shows the global effect of heat and mass diffusion, and of heat release.

The competition between the previous mechanisms is clearer when looking at the axial profiles in Figure 6 sampled along the stoichiometric Bilger mixture fraction [31]. Up to 1 mm downstream of the bluff-body both heat diffusion and H_2 preferential mass diffusion control the stabilization by enhancing preheating and mixing of reactants. Downstream and up to about 2 mm the H_2 diffusion is still faster than convection. Further downstream convective transport dominates. In the same Figure 6, it is also possible to note the roll-up produced at instant 1 by vortex shedding at about 5 mm from injection.

4.1.1. *Importance of preferential diffusion*

In simulations of the present work, each chemical species has its own diffusion coefficient, D_i, into the rest of mixture. In this way the preferential diffusion effect is taken into account. The diffusion coefficient D_i is estimated by means of the simplified expression

$$D_i = \frac{1 - Y_i}{\sum_{j=1,\, j\neq i}^{N_s} \frac{X_j}{\mathcal{D}_{ji}}}, \tag{22}$$

first proposed by Stefan [33] and then used by Hirschfelder and Curtiss in their diffusion model [16]. In this expression, Y_i and X_j are the mass and molar fractions of the i-th and j-th chemical species, respectively, N_s is the number of species and $\mathcal{D}_{ji}$ are the binary mass diffusivities for all pairs of species in the mixture. The $\mathcal{D}_{ij}$ are explicitly predicted by kinetic theory [15, p. 525–528], [34, p. 168].

The diffusive fluxes are modelled according to the Hirschfelder–Curtiss law (23),

$$\boldsymbol{J}_i = -\rho Y_i D_i \frac{\nabla X_i}{X_i}, \tag{23}$$

neglecting the Soret contribution to mass diffusive fluxes.

It is observed that the diffusion coefficient D_i is an effective diffusion coefficient of the i-th species into the mixture (mixture-average assumption). Since this is a zeroth-order model [35], it neglects some physics in the diffusion process (in particular, cross-diffusion, the Soret and Dufour effects); hence, adding up all species diffusion fluxes does not yield zero, and mass conservation is no longer automatically ensured. This problem requires a particular treatment of diffusive fluxes described in [18].

Preferential diffusion in turbulent flows is usually negligible in the major part of the field with respect to turbulent stirring which is sufficiently strong to make the effective turbulent diffusivity nearly equal for all scalars. However, it can't usually be neglected close to injection, as reported in [36] for nitrogen-diluted H_2 flames and in [37] for $CH_4/H_2/N_2$ flames. Furthermore, recent results show that thermo-diffusive mechanisms (associated to preferential diffusion) could be the source of additional wrinkling in turbulent flames [38].

The importance of preferential diffusion of molecular hydrogen in the anchoring of the flame studied in this work was stressed in Section 4.1 looking at characteristic times. The relevance of preferential diffusion in the flow can also be shown with a different analysis. The degree of differential diffusion may be quantified by looking at elemental mixture fractions. For example, for the syngas–air non-premixed flame simulated here with accurate calculation of diffusion coefficients by means of kinetic theory, two mixture fractions for hydrogen and carbon can be defined:

$$F_H = \frac{Y_H - Y_{H,1}}{Y_{H,2} - Y_{H,1}} \qquad \text{and} \qquad F_C = \frac{Y_C - Y_{C,1}}{Y_{C,2} - Y_{C,1}}, \tag{24}$$

where subscripts 1 and 2 refer to fuel and air streams, respectively. A differential diffusion parameter can then be defined as the difference of these elemental mixture fractions, $Z_{\text{Pref. Diff.}} = F_H - F_C$, shown in Figure 7. This picture shows a small portion of the averaged flowfield (RED_{ZOOM} case) close to the nozzle and shows that preferential diffusion cannot be neglected in this region.

Preferential diffusion can lead to thermo-diffusive instability depending on the ratio between the thermal and mass diffusivity of reactants, i.e. the so-called Lewis number, $Le_i = \alpha / D_i$ [18]. When $Le_i < 1$, as in the case of hydrogen, some thermo-diffusive instabilities [39, p. 357–365], [40] may grow and increase the flame surface and global burning rate [41, p. 56–59], [42, 43], up to the formation of cellular flames when the flow is laminar [39, p. 349–365]. It is observed that laminar flame instabilities are enhanced by lower Lewis numbers and by increasing pressure [44]; a complete discussion about instability mechanisms in laminar flames can be found in [39, 45]. Recently it has been observed that the effect of the Lewis number on the reaction rate and flame propagation is present not only in laminar flames but also in turbulent flames [38]. In fact, since the leading edges of the flame brush have mostly positive curvature (convex to fresh reactants),

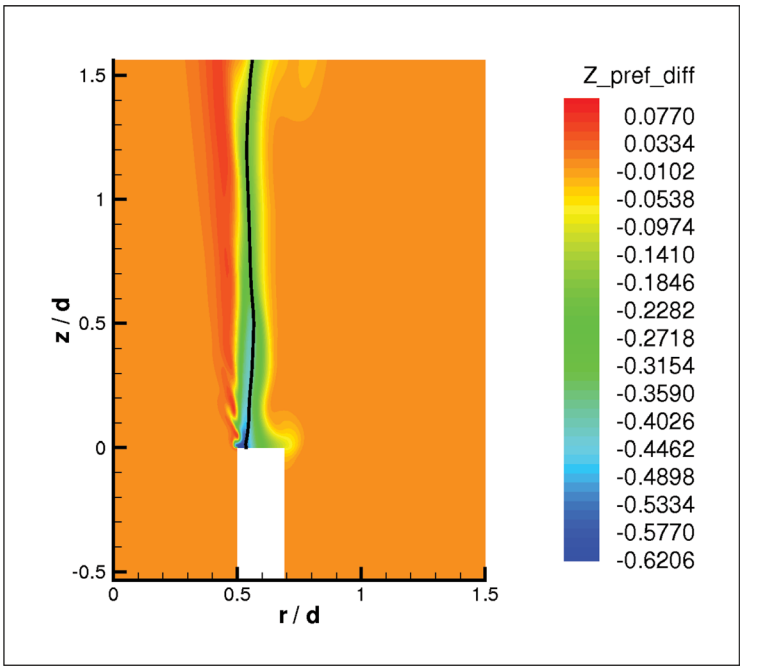

Figure 7. Degree of preferential diffusion close to the injection predicted in the RED_{ZOOM} simulation. The black line is the stoichiometric Bilger mixture fraction [31] line for this flame. Spatial coordinates are non-dimensionalized by means of the nozzle diameter, d.

they can reveal the effects of the differences among the molecular transport properties of fuel, oxidizer, and heat, in high turbulent flows. Also DNS studies showed similar results on flame propagation [40].

It was observed that the very tight wall of the nozzle tubing (the thickness is 0.88 mm) is sufficient to stably anchor the actual flame in the experiment. Numerical RED_{ZOOM} simulation shows that very small vortices downstream of the tubing contribute to flame stabilization. Furthermore, also hydrogen preferential diffusion ($Le_{H_2} < 1$) plays an important role in anchoring this flame by enhancing mixing of hydrogen and hot products. No thermo-diffusive instabilities develop, probably controlled by the sufficiently high jet Reynolds number.

4.2. *Analysis of the whole flame dynamics*

To simulate the whole flame with a coarser computational grid, an artificial stabilization mechanism is needed. It is developed based on results of the RED_{ZOOM} case. Since the Chen chemical mechanism is not self-starting, i.e. high temperature alone is not sufficient to activate reactions, also a non-zero distribution of some radical species must be prescribed to ignite the mixture. In particular, since H radical formation is found to be critical for the activation of the Chen mechanism, and since its characteristic production time scales are generally shorter than the other radical species considered in these simulations (O and OH), as shown in Figure 4, the time averaged H production rate is modelled and taken constant in time over a small region ($\sim$2 mm long and $\sim$ 0.15 mm radially wide) immediately downstream of the bluff-body. It is observed that the axial extension of this region is nearly the extension of the region where the H_2 mass diffusion time scales are shorter than convective time scales (see Figure 6). The value of the averaged H

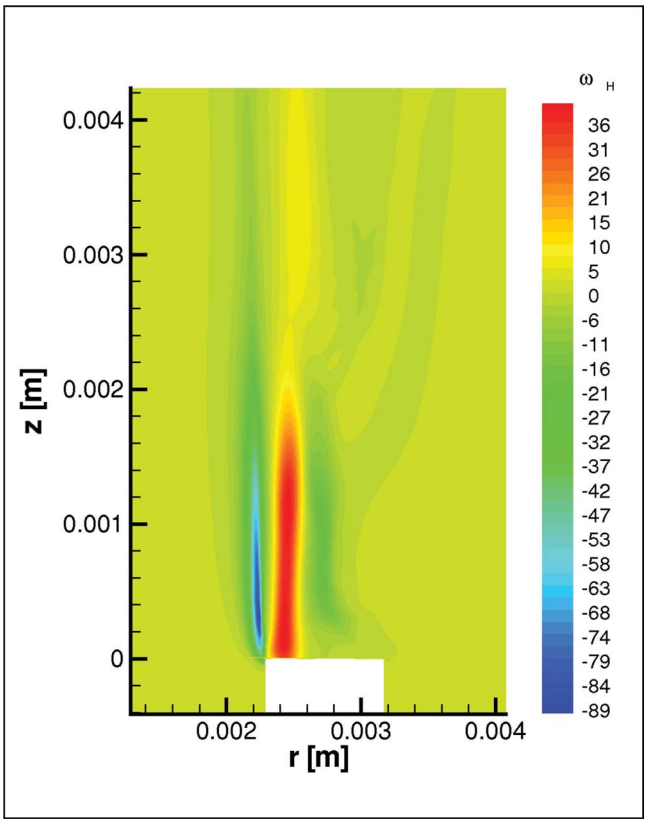

Figure 8. Detail of the average H source rate, $\dot{\omega}_{\mathrm{H}}$, predicted by the $\mathrm{RED}_{\mathrm{ZOOM}}$ simulation.

production rate as calculated in the $\mathrm{RED}_{\mathrm{ZOOM}}$ simulation and shown in Figure 8 is scaled on the coarser grid to maintain the local Damköhler number: $\omega_{H,\mathrm{coarse}} \sim \omega_{H,\mathrm{fine}} \cdot \Delta_{\mathrm{fine}}/\Delta_{\mathrm{coarse}}$ (Δ being the local size of the grid), which decreases $\omega_{H,\mathrm{fine}}$ by a factor of 10.

The stabilization mechanism assumed was derived from the $\mathrm{RED}_{\mathrm{ZOOM}}$ results close to the injector. Despite this, it remains an artificial stabilization mechanism and it is coupled with a lower spatial resolution grid in the other RED simulations. Hence, the flame dynamics close to the injector is expected to be different. In fact, while the flame in the $\mathrm{RED}_{\mathrm{ZOOM}}$ simulation is anchored at the inner edge of the bluff-body (see Figure 1), in the RED_C simulation the flame anchors at the outer edge (see Figures 9 and 10). This is supposed to be related to the loss of fluid dynamic details in the injection region, that in particular results in shedding of larger coherent structures, roughly double-sized in the RED_C case with respect to the $\mathrm{RED}_{\mathrm{ZOOM}}$ case. Both Figures 9 and 10 show that a stable flame, ~5 mm long and well attached to the bluff-body, seems to act as a pilot, thus providing continuous ignition of reactants. This results in an average continuous and attached flame (see Figure 10, on the right).

Figure 9 reports a time sequence of temperature fields, with a delay time $\Delta\tau = 1.2$ ms between each frame, and shows that the numerical flame experiences some localized extinctions and re-ignitions. Hot pockets of products are released from the anchoring region, accelerate driven by buoyancy, and then ignite the unburnt mixture downstream. These isolated 'tongues' are marked as A, B, C, A′, . . . , and collapse to a unique flame front at ~10 cm from the injection. It can be noted that similar structures reach the same axial location after a delay time of ~2–3 $\Delta\tau$.

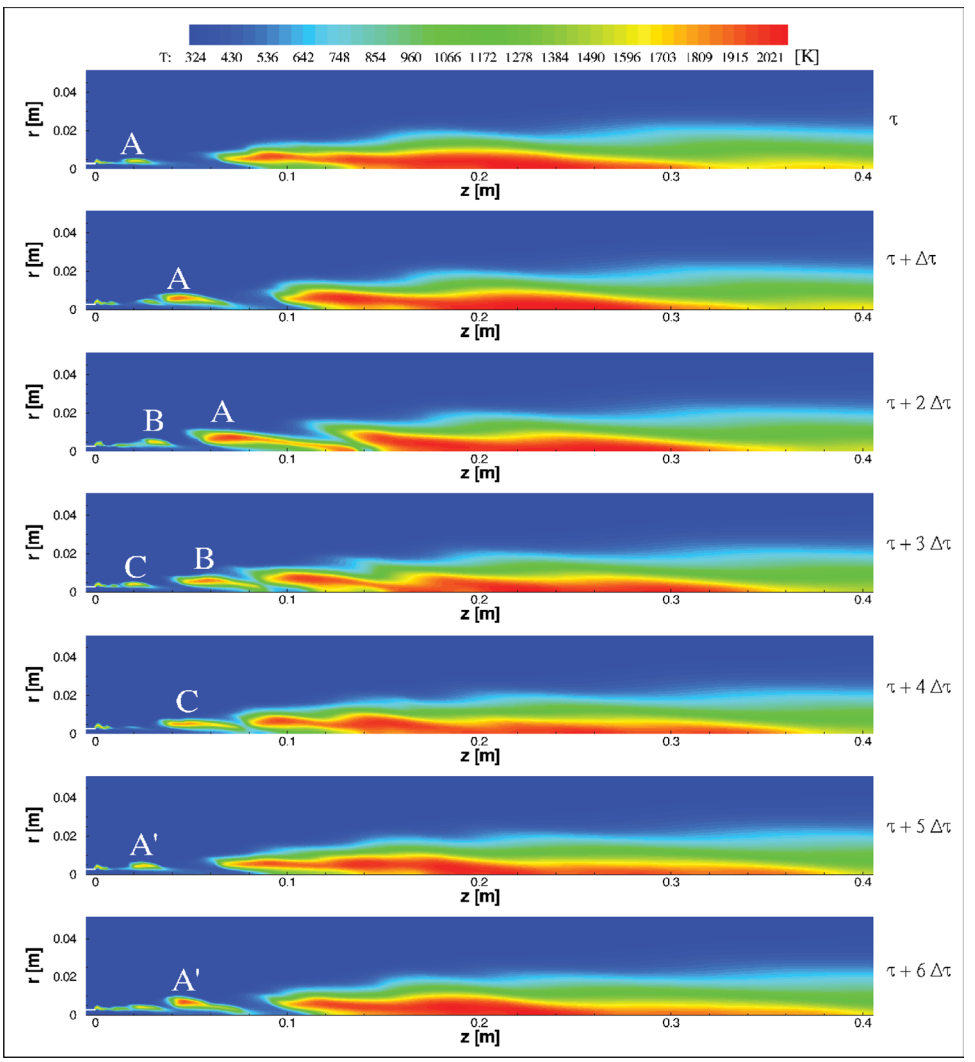

Figure 9. Sequence of instantaneous temperature fields for the RED_C simulation, with $\Delta\tau = 1.2$ ms. Recall that the flame is vertically posed, although horizontally shown in this picture.

This delay time is in agreement with the fundamental frequency (∼330 Hz) revealed by the temperature spectrum sampled at point $m4$, located in a region influenced by the flame tongues motion (see Figure 10), and reported in Figure 11(a). The motion of these flame tongues, in terms of frequency peaks, is also revealed but with smaller amplitude by the temperature spectrum at point $m5$, located on the axis of symmetry and more downstream of point $m4$.

These periodic oscillations and flame tongues are due to the velocity fluctuations close to the injection region, i.e. the vortex shedding. The characteristic frequencies of these fluctuations are given by the kinetic energy spectrum peaks at point m_{12} (the closest to the bluff-body among the three points chosen for sampling) in Figure 11(b). The main peak reveals that vortex shedding takes place at ∼9 kHz, which is of the same order of magnitude as that obtained in the RED_{ZOOM} simulation, although the coherent structures released are larger. The same kinetic energy spectrum

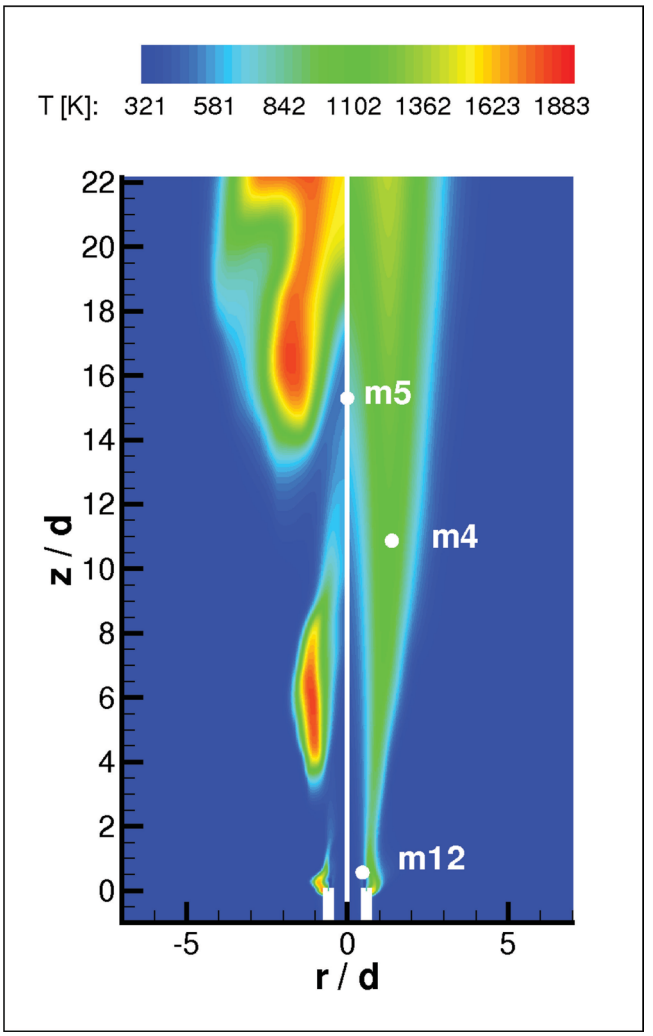

Figure 10. RED_C simulation results. A zoomed-in view of an instantaneous temperature field (on the left) and of the averaged temperature field (on the right) is shown. The white points indicate the sampling points to which the spectra of Figure 11 refer. Spatial coordinates are non-dimensionalized by means of the nozzle diameter, $d = 4.58$ mm.

at point m_{12} shows also a minor peak at ~18 kHz, likely related to acoustic fluctuations induced by the vortex shedding. These two peaks are also present with smaller amplitudes in the temperature spectrum at point m_{12}. This shedding rapidly affects the local velocity and acoustic dynamics, but not the local temperature dynamics. In fact, the ~9 and ~18 kHz peaks in the temperature spectrum have a reduced amplitude. Moreover, reacting 'tongues' appear more downstream at a frequency of ~330 Hz, which is much lower than that of the alternate vortex shedding from the edges of the bluff-body, ~9 kHz. It is observed that this 330 Hz frequency of the flame 'tongues' is in agreement with their axial convective velocity and their 'spatial wavelength', λ, given by the average distance between two consecutive 'tongues' passing over the point $m4$. From Figures 9 and 10 it is found that $\lambda \sim 4 \cdot 10^{-2}$ m. Hence, since $f = U_c/\lambda$ and $f \sim 330$ Hz, then

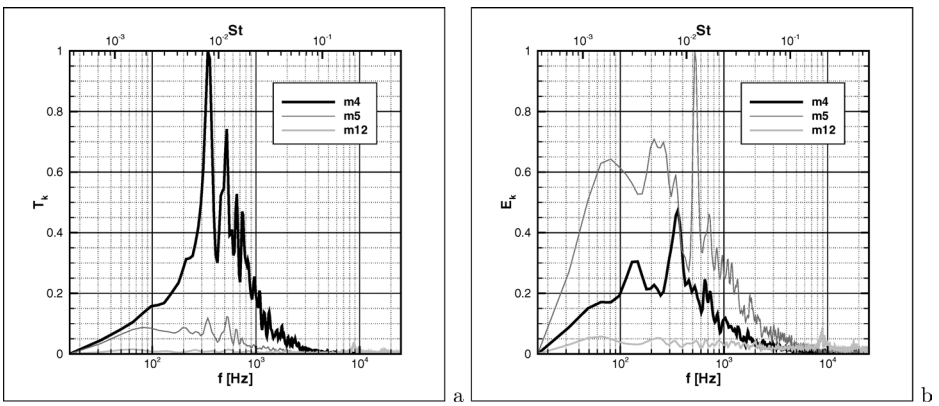

Figure 11. Temperature (Figure 11a) and kinetic energy (Figure 11b) normalized spectra obtained at certain locations (shown in Figure 10) in the RED_C simulation. The amplitude of the Fourier components T_k and E_k were normalized by means of the associated peak values shown in the figures. The upper horizontal axis shows the Strohual number, $St = ft/U_m$, f being the frequency, $t = 0.88$ mm the thickness of the fuel pipe, and U_m the average of the bulk velocities of the two coaxial jets.

$U_c \sim 13\,\mathrm{m\,s^{-1}}$. This average convective velocity of flame 'tongues' is in close agreement with a rough estimation from Figure 9: in fact, the spatial distance between the head of 'tongue B' in the third frame and the same head in the fourth frame is $\sim 1.8 \cdot 10^{-2}$ m, and considering that the delay time between the two frames is $1.2 \cdot 10^{-3}$ s, the convective velocity of 'tongue B' is $\sim 15\,\mathrm{m\,s^{-1}}$.

Figure 11 shows temperature and kinetic energy spectra at points m_4, m_5 and m_{12} also in terms of the non-dimensional Strohual number, $St = ft/U_m$, where f is the frequency, t is the thickness of the fuel pipe ($0.88 \cdot 10^{-3}$ m) separating the two coaxial fuel and air jets, and U_m the average of the bulk velocities of the two jets (76 and $0.75\,\mathrm{m\,s^{-1}}$, respectively). The $\sim$9 kHz frequency peak associated to the vortex shedding corresponds to $St \sim 0.21$, which is close to $St = 0.24$ commonly found experimentally for vortex shedding in axisymmetric pipes [46]. According to [46], a non-reacting coaxial jet configuration experiences vortex shedding from the inner duct wall for $U_i/U_o \geq 0.44$, with a frequency f defined by constant $St = 0.24$: U_i and U_o are the inner and outer velocities and St the Strouhal number defined as above. The present configuration is characterized by $U_i/U_o \sim 101$. If $St = 0.24$ was assumed also at this velocity ratio, the resulting shedding frequency would be $\sim$10 466 Hz which is closer to the $\sim$11 kHz predicted by the $\mathrm{RED}_{\mathrm{ZOOM}}$ simulation, not influenced by any artificial flame anchoring mechanism.

4.2.1. *Averaged results*

All the simulations of the whole flame predict a continuous and well attached averaged flame, as shown in Figures 10 and 12 for the RED_C case as an example. The black line in Figure 12 is the stoichiometric Bilger mixture fraction ($F^{\mathrm{st}}_{\mathrm{BLGR}} = 0.295$) [31] that is used to measure the stoichiometric flame length, L_{stoich}. According to experiments, $L_{\mathrm{stoich}} = 47\,d$, d being the fuel jet diameter. Considering that systematic errors in the detection of chemical species ranges from 3 to 15 %, with an error of 10%, then $L_{\mathrm{stoich}} \sim 42.3$–$51.7\,d$. The stoichiometric flame length predicted in the RED_C case is $L_{\mathrm{stoich}} = 42.5\,d$, in reasonable agreement with measurements.

In the FAST case the agreement with measurements in terms of average quantities is good only for temperatures at experimental stations close to the nozzle exit (the first two, 'a' and 'b', of

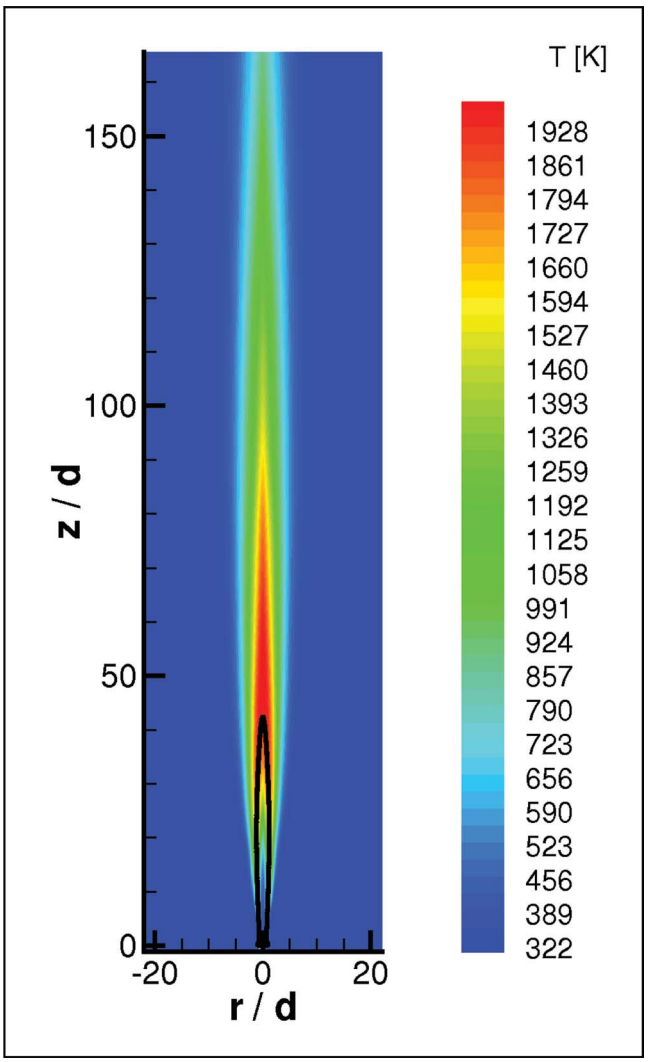

Figure 12. RED_C simulation results in terms of the averaged temperature field and the stoichiometric Bilger mixture fraction ($F^{st}_{BLGR} = 0.295$) [31]. Spatial coordinates are non-dimensionalized by means of the nozzle diameter, $d = 4.58$ mm.

Figure 13), where, however, H_2O is overpredicted (see Figure 14) and CO_2 largely underpredicted (see Figure 15). This is expected due to the assumptions about the two chemical mechanisms of the FAST case. In fact, hydrogen consumption is overpredicted since there is no activation energy to control it; the only limiting factor is the fluid dynamic mixing imposed via Equation (7). Consequently, oxygen consumption is mainly due to this reaction and thus the CO oxidation is underpredicted. The CO_2 underprediction might also be due to an underestimation of the turbulent mixing due to the lack of three-dimensional effects; in fact, the predicted rms fluctuations are much lower than experimental data (hence, they are not reported in this work which is preliminary to a fully three-dimensional LES). The underprediction of turbulent mixing would apply also to the RED cases. Downstream, the average temperature is underpredicted; H_2O is overpredicted,

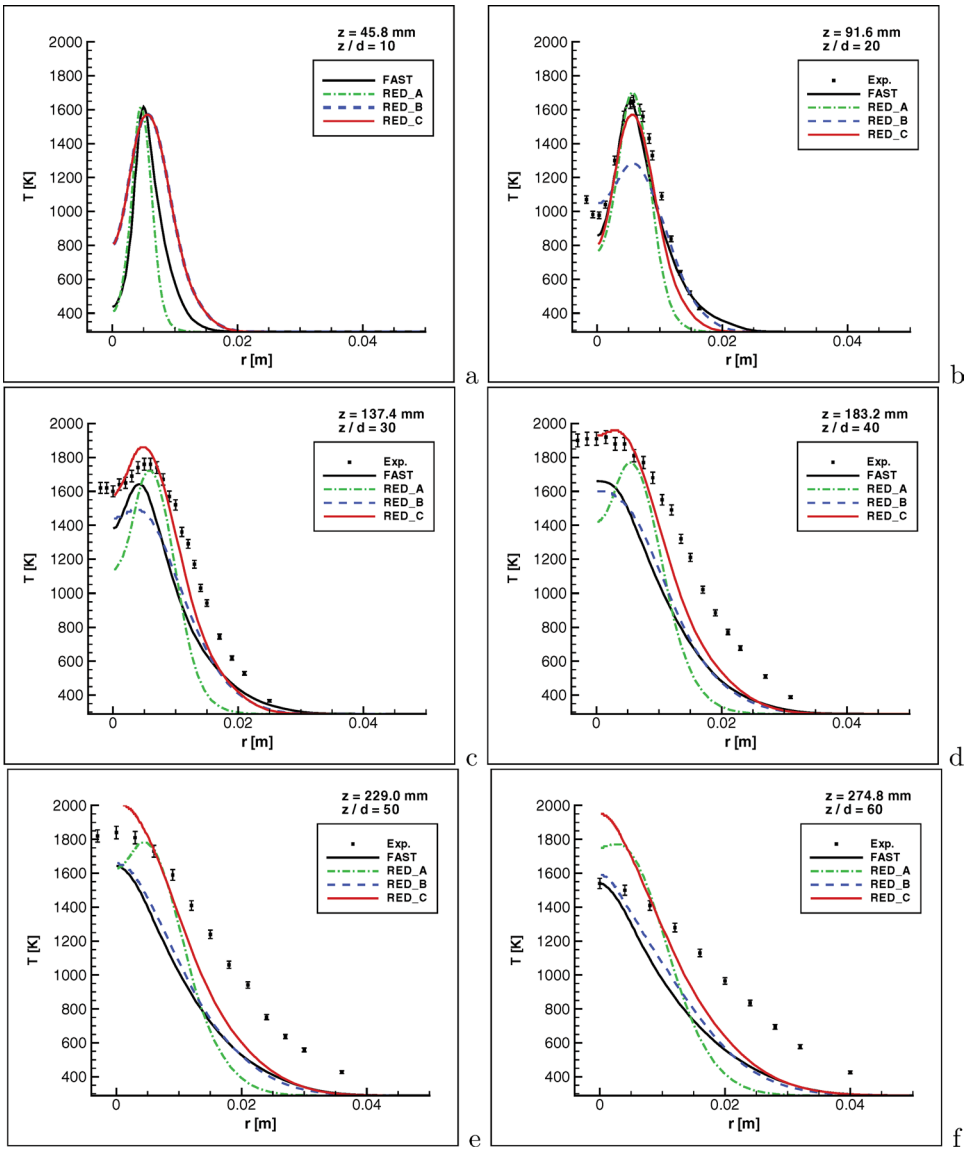

Figure 13. Comparison of numerical temperature radial profiles predicted in the present simulations with experimental data at different axial locations.

especially close to the axis; this overestimation decreases at last two stations ('e' and 'f'); CO oxidation remains strongly underestimated.

The RED_A and RED_B cases differ only in the FM constant, σ_{FM}, which is 0.2 and 0.35, respectively. Comparing the RED_A and RED_B radial profiles in Figures 13–15, it can be deduced that combustion is more efficient in the RED_A case, due to the higher temperature and product (especially H_2O) concentrations. These results are justified by the lower σ_{FM}, which decreases the damping of turbulent fluctuations and enhances turbulent mixing. The increased diffusion in

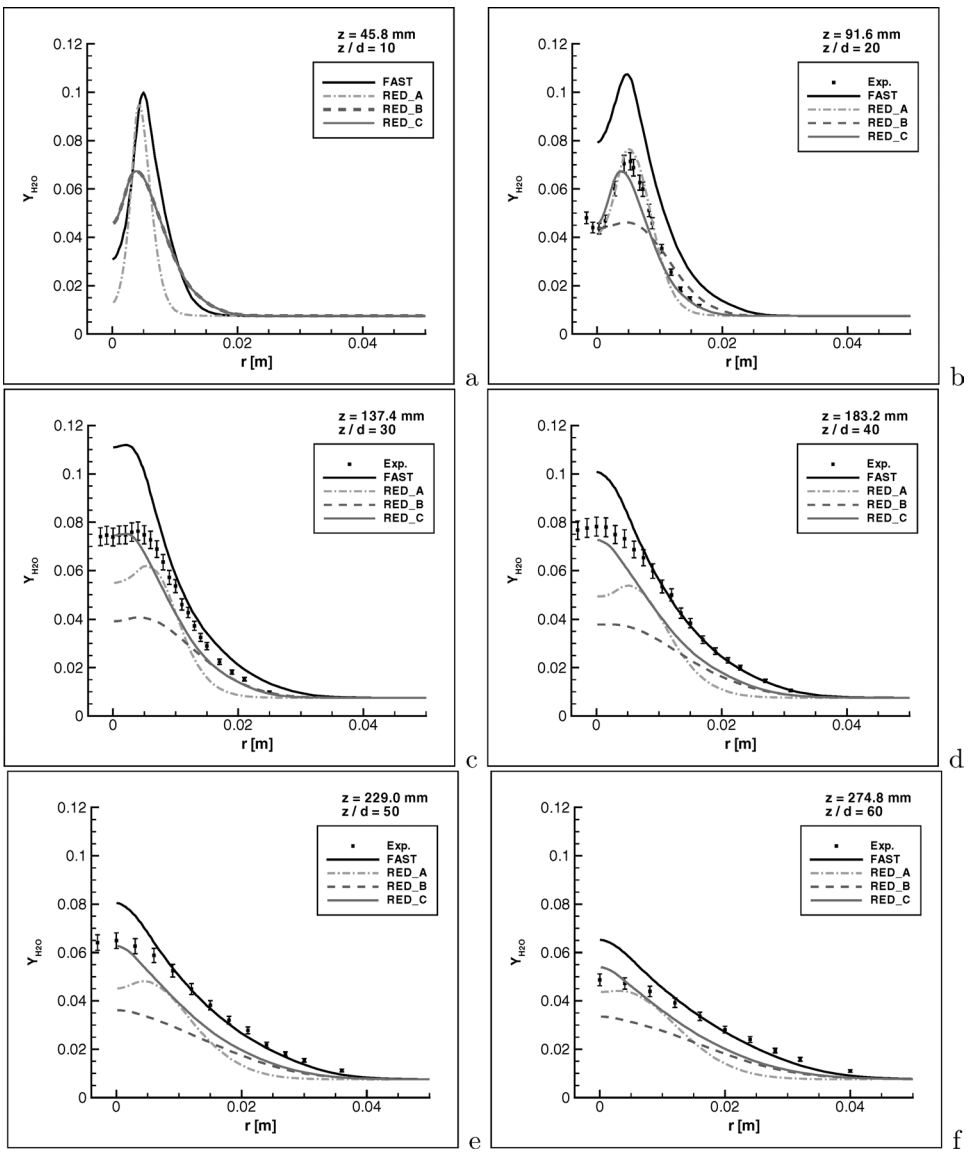

Figure 14. Comparison of numerical H_2O mass fraction radial profiles with experimental data at different axial locations.

the RED_B case is also shown by the increased radial penetration of the scalars shown in Figures 13–15.

The RED_B and RED_C cases have the same $\sigma_{\mathrm{FM}} = 0.35$, but different maximum radial extension of the computational domain. In particular, the RED_C domain is ∼2.18 times larger than RED_B. It is observed that in the RED_C case the flame reaches higher temperatures and is longer than the RED_B case. The 'numerical' interaction between the flame and the lateral boundary condition (CLOAK) is expected to decrease with increasing the radial extension of the computational

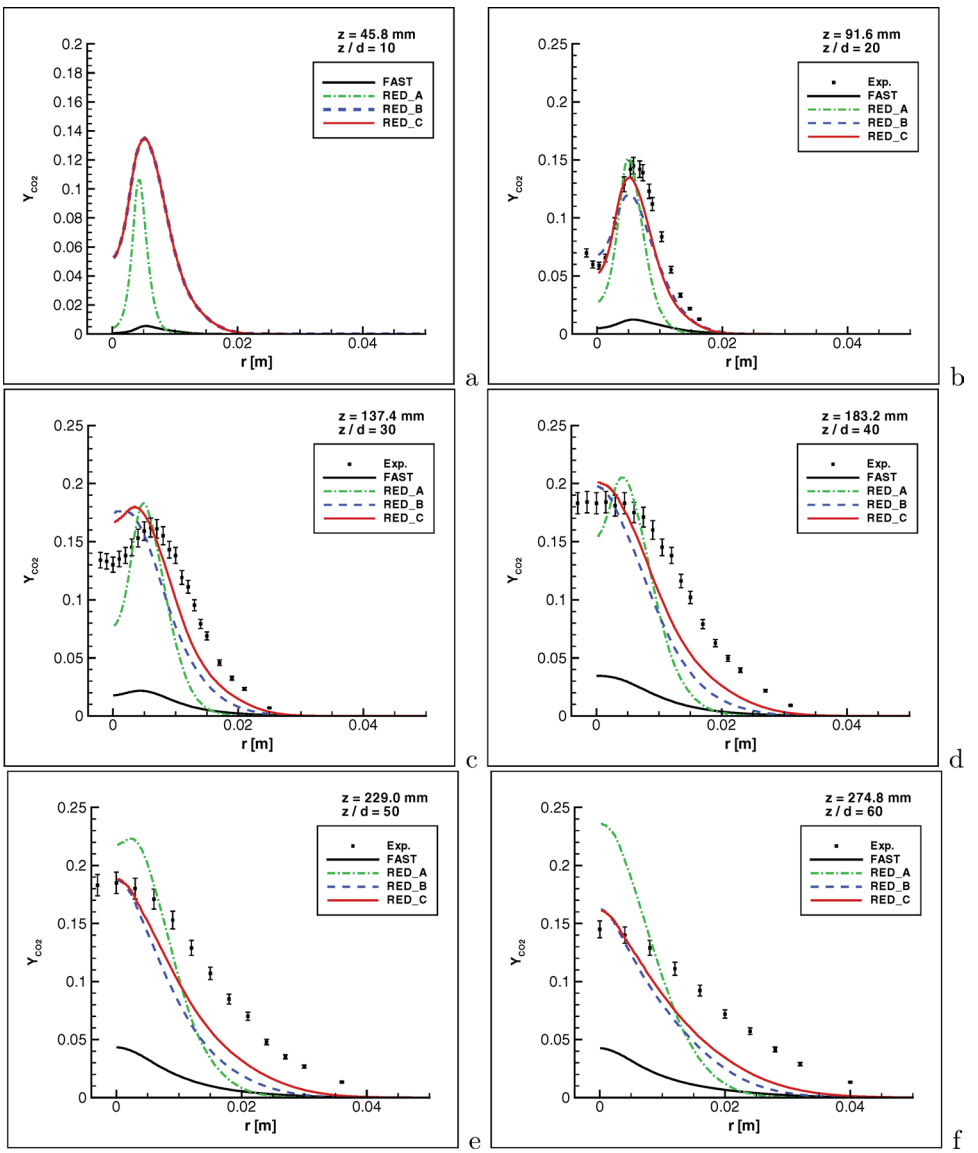

Figure 15. Comparison of numerical CO_2 mass fraction radial profiles with experimental data at different axial locations.

domain, i.e. in the RED_C case. In fact, comparing the profiles in Figures 13–15 it seems that the RED_B flame suffers from a confinement-like effect that shortens it.

5. Conclusions

The Sandia/ETH-Zurich $CO/H_2/N_2$ non-premixed unconfined turbulent jet flame (named 'Flame A') is numerically simulated by solving the unsteady compressible reactive Navier–Stokes equations in a three-dimensional axisymmetric formulation, hence, in a formally two-dimensional domain. Chemical kinetics implemented range from very simple to complex, including the main

radical species required to capture non-equilibrium phenomena like localized extinctions and re-ignitions.

The actual flame is well anchored in the experiments without requiring a pilot, although the nozzle thickness acting as a bluff-body is very tight. The present simulations confirm the expectations of experimentalists about the existence of a small recirculation zone producing the anchoring of the flame. In particular, results show that the flow experiences high frequency alternate vortex shedding from the squared-off ends of the nozzle. It is observed that this is critical to stabilizing the flame in numerical simulations with realistic chemistry. This stresses the strong interaction between turbulence and combustion in the injection region. Results also show the importance of preferential diffusion in enhancing mixing between reactants especially in the zone where vortex shedding takes place.

The study of the anchoring of this flame shows that syngas may easily result in attached flames. From a practical point of view, this is a warning for designers and for people converting old plants, before fed with different fuels, to use syngas.

Since the computational code used for the present simulations works with structured grids, an artificial stabilization mechanism was developed based on results close to the injection obtained on a small domain with a very fine grid. This mechanism was then used to simulate the whole flame on coarser grids.

Different simulations were performed to check the effects of boundary conditions. Averaged results were compared with experimental data and unsteady results described for the most representative case. In particular, a well stabilized flame, acting as a pilot, is found to be attached to the bluff-body, from which alternate vortex shedding takes place at ∼9 kHz. In this region preferential diffusion is also found to be important, hence, it may play a critical role in the anchoring. From the stabilization region some hot spots are released at ∼330 Hz, and these react downstream resulting in 'tongues' collapsing to a unique flame front at a certain axial distance from the injector.

Having tested the effects of spatial resolution, chemistry and boundary conditions, the present results will be used as a starting point for a fully three-dimensional LES computation, to better investigate and understand the turbulence–combustion interaction, especially close to the injection region. In particular, the present results suggest we compute dynamically the constant σ_{FM}, thus avoiding its empirical choice, and to widen the radial computational domain to reduce the influences of lateral (CLOAK) boundary conditions on the flame.

References

[1] B.J. Boersma, *Direct Numerical Simulation of a Turbulent Reacting Jet*, Center for Turbulence Research, Annual Research Briefs, 1999.

[2] R.S. Barlow, SANDIA/ETH-Zurich $CO/H_2/N_2$ Flame Data – Release 1.1, www.ca.sandia. gov/TNF, Sandia National Laboratories, 2002.

[3] R.S. Barlow, G.J. Fiechtner, C.D. Carter, J.Y. Chen and J. Gore, *Experiments on the scalar structure of turbulent $CO/H_2/N_2$ jet flames*, Combust. Flame 120 (2000), pp. 549–569.

[4] E. Giacomazzi, C. Bruno and B. Favini, *Fractal modeling of turbulent combustion*, Combust. Theory Model. 4 (2000), pp. 391–412.

[5] E. Giacomazzi, C. Bruno and B. Favini, *Fractal modeling of turbulent mixing*, Combust. Theory Model. 3 (1999), pp. 637–655.

[6] E. Giacomazzi, V. Battaglia and C. Bruno, *The coupling of turbulence and chemistry in a premixed bluff-body flame as studied by LES*, Combust. Flame 138 (2004), pp. 320–335.

[7] ENEA – Progetto Telegrid: Principali Risorse di Calcolo in ENEA, Italian Agency for New Technologies, Energy and Environment. http://www.telegrid.enea.it.

[8] B. Engquist, P. Lotstedt and B. Sjogreen, *Nonlinear filters for efficient shock computation*, Math. Comput. 52 (1989), pp. 509–537.

[9] E. Giacomazzi, B. Favini, C. Bruno, F.R. Picchia and N. Arcidiacono, *LES of H_2/CH_4/Air turbulent non-premixed flame*, in *European Combustion Meeting*, 25–28 October, Orleans, France, Iskander Gokalp, ed., 2003. http://www.gfcombustion.asso.fr/ecm.php?langue=en.

[10] R. Potami, E. Giacomazzi, B. Favini, F.R. Picchia and N. Arcidiacono, *Mixture preheating effects in a bluff-body burner*, in *XXVI Event of the Italian Section of the Combustion Institute*, Ischia, Italy, 18–21 September, 2003. http://www.combustioninstitute.it

[11] M. Germano, U. Piomelli, P. Moin and W.H. Cabot, *A dynamic subgrid-scale eddy viscosity model*, Phys. Fluids A 3 (1991), pp. 1760–1765.

[12] B.F. Magnussen, *The Eddy Dissipation Concept for Turbulent Combustion Modeling. Its Physical and Practical Implications*, Technical Report number N-7034, Division of Thermodynamics, Norwegian Institute of Technology, Trondheim, Norway, 1989.

[13] A. Ern and V. Giovangigli, *Multicomponent Transport Algorithms*, Lecture Notes in Physics, Vol. M24, Springer-Verlag, Heidelberg, 1994.

[14] A. Ern and V. Giovangigli, *Fast and accurate multicomponent transport property evaluation*, J. Comput. Phys. 120 (1995), pp. 105–116.

[15] R.B. Bird, W.E. Stewart and E.N. Lightfoot, *Transport Phenomena*, 2nd edition, John Wiley, New York, 2002.

[16] J.O. Hirschfelder, C.F. Curtiss, R.B. Bird and E.L. Spotz, *The Molecular Theory of Gases and Liquids*, John Wiley, New York, 1954.

[17] C.R. Wilke, J. Chem. Phys. 18 (1950), pp. 517–519.

[18] E. Giacomazzi, F.R. Picchia and N. Arcidiacono, *A review of chemical diffusion, criticism and limits of simplified methods for diffusion coefficients calculation*, Combust. Theory Model. 12 (2008), pp. 135–158.

[19] C.D. Pierce, *Progress-variable approach for large-eddy simulation of turbulent combustion*, PhD thesis, Department of Mechanical Engineering, Stanford University, 2001.

[20] S.R. Turns, *An Introduction to Combustion. Concepts and Applications*, 2nd edition, McGraw-Hill, New York, 2000.

[21] C.T. Bowman, *Chemistry of gaseous pollutant formation and destruction*. In: *Fossil Fuel Combustion: A Source Book*, 2nd edition, W. Bartok and A.F. Sarofim, eds., John Wiley, New York, 1991.

[22] I. Glassman, *Combustion*, 3rd edition, Academic Press, San Diego, 1996.

[23] E. Giacomazzi, *Modellistica e simulazione della combustione turbolenta*, PhD thesis, Department of Mechanics and Aeronautics, University of Rome La Sapienza, 2000.

[24] B.R. Adams, M.A. Cremer and D.H. Wang, *Modeling non-equilibrium CO oxidation in combustion systems*, in *International Mechanical Engineering Congress & Exposition*, Orlando, Florida, 5–10 November, 2000.

[25] F.L. Dryer and I. Glassman, *High temperature oxidation of CO and CH_4*, in *Fourteenth Symposium (International) on Combustion*, The Combustion Institute, Pittsburg, 1972, p. 987.

[26] T.J. Poinsot and S.K. Lele, *Boundary conditions for direct simulations of compressible viscous flows*, J. Comput. Phys. 101, (1992), pp. 104–129.

[27] W. Polifke and C. Wall, *Non-reflecting boundary conditions for acoustic transfer matrix estimation with LES*, in *Center for Turbulence Research, Proceedings of Summer Program*, Stanford, 2002.

[28] P. Orlandi, *Fluid Flow Phenomena—A Numerical Toolkit*, Kluwer Academic, Dordrecht, 2000.

[29] P. Orlandi and S. Leonardi, *Passive scalar in a turbulent channel flow with wall velocity disturbances*, Flow, Turbul. Combust. 72 (2004), pp. 181–197.

[30] F. Picano, G. Troiani and C.M. Casciola, *Effects of inflow conditions on premixed reactive turbolent annular jet*, in *XVIII Congresso AIMETA*, Brescia, Italy, 11–14 September, 2007.

[31] R.W. Bilger, S.H. Starner and R.J. Kee, *On reduced mechanisms for methane–air combustion in nonpremixed flames*, Combust. Flame 80 (1990), pp. 135–149.

[32] R. Borghi and M. Destriau, *La Combustion et les Flammes*, Editions Technip, Paris, 1995.

[33] J. Stefan, Sitzungsberichte Akad. Wiss. Wien II(68)(1874), p. 325.

[34] K.K. Kuo, *Principles of Combustion*, John Wiley, New York, 1986.

[35] V. Giovangigli, *Multi-Component Flow Modeling*, Birkhauser, Boston, 1999.

[36] W. Meier, A. Vydorov, V. Bergmann and W. Stricker, *Simultaneous Raman/LIF measurements of major species and NO in turbulent H_2/air diffusion flames*, Appl. Phys. B 63 (1996), pp. 79–90.

[37] V. Bergmann, W. Meier, D. Wolff and W. Stricker, *Application of spontaneous Raman and Rayleigh scattering and 2D LIF for the characterization of a turbulent $CH_4/H_2/N_2$ jet diffusion flame*, Appl. Phys. B, 66 (1998), pp. 489–502.

[38] A.N. Lipatnikov and J. Chomiak, *Molecular transport effects on turbulent flame propagation and structure*, Prog. Energy Combust. Sci. 31 (2005), pp. 1–73.
[39] F.A. Williams, *Combustion Theory*, 2nd edition, Addison-Wesley, Boston, 1985.
[40] A. Trouve and T. Poinsot, *The evolution equation for the flame surface density*, J. Fluid Mech. 278 (1994), pp. 1–31.
[41] J. Chomiak, *Flame Propagation in Laminar Flows*, in *Combustion: A Study in Theory, Fact and Application*, A.K. Gupta and D.G. Lilley, eds., Abacus Press/Gordon and Breach Science Publishers, New York, 1990.
[42] J. Buckmaster, *The quenching of a deflagration wave held in front of a bluff body*, in *Seventeenth Symposium (International) on Combustion*, The Combustion Institute, Pittsburg, 1979, pp. 835–842.
[43] J. Buckmaster and F.A. Mikolaitis, *A flammability-limit model for upward propagation through lean methane/air mixtures in a standard flammability tube*, Combust. Flame 45 (1982), pp. 109–119.
[44] X.J. Gu, M.Z. Haq, M. Lawes and R. Woolley, *Laminar burning velocity and Markstein lengths of methane–air mixtures*, Combust. Flame 121 (2000), pp. 41–58.
[45] P. Clavin, *Dynamic behaviour of premixed flame fronts in laminar and turbulent flows*, Prog. Energy Combust. Sci. 11 (1985), pp. 1–59.
[46] G. Buresti, A. Talamelli and P. Petagna, *Experimental characterization of the velocity field of a coaxial jet configuration*, Exper. Therm. Fluid Sci. 9 (1994), pp. 135–146.